PCCP

Static ^{1}H Dynamic Nuclear Polarization with the biradical TOTAPOL: a transition between the solid effect and the cross effect

Journal:	*Physical Chemistry Chemical Physics*
Manuscript ID:	CP-ART-12-2013-055504.R1
Article Type:	Paper
Date Submitted by the Author:	05-Feb-2014

Complete List of Authors:	Shimon, Daphna; Weizmann Institute of Science, Chemical Physics Feintuch, Akiva; Weizmann Institute of Science, Chemical Physics Goldfarb, Daniella; Weizmann Institute of Science, Chemical Physics Vega, Shimon; Weizmann Institute of Science, Chemical Physics

Static ^{1}H Dynamic Nuclear Polarization with the biradical TOTAPOL: a transition between the solid effect and the cross effect

Abstract

To study the solid ^{1}H-DNP mechanism of the biradical TOTAPOL under static conditions the frequency swept DNP enhancement spectra of samples containing 20 mM and 5 mM TOTAPOL were measured as a function of MW irradiation time and temperature. We observed that under static DNP conditions the biradical TOTAPOL behaves similar to the monoradical TEMPOL, in contrast to MAS DNP where TOTAPOL is considerably more effective. As previously done for TEMPOL, the TOTAPOL DNP spectra were analyzed taking a superposition of a basic SE-DNP lineshape and a basic CE-DNP lineshape with different amplitudes. The analysis of the steady state DNP spectra showed that the SE was dominant in the 6-10 K range and the CE was dominant above 10K. DNP spectra obtained as a function of MW irradiation times allowed resolving the individual SE and CE buildup times. At low temperatures the SE buildup time was faster than the CE buildup time and at all temperatures the CE buildup time was close to the nuclear spin-lattice relaxation time, T_{1n}. Polarization calculations involving nuclear spin-diffusion for a model system of one electron and many nuclei suggested that the shortening of the T_{1n} for increasing temperatures is why the SE contribution to the overall enhancement was reduced.

1 Introduction

In recent years Dynamic Nuclear Polarization (DNP) has become a frequently used method to enhance NMR signals. It is based on polarization transfer from radicals added to the NMR samples, theoretically, leading to a maximal enhancement of the NMR signal that is equal to the ratio between the electron and nuclear gyromagnetic ratios, γ_e/γ_n, which is ~660 for ^{1}H and ~2640 for ^{13}C [1].

Traditionally, three main mechanisms are used to describe DNP in the solid state and they can be classified according to the number of electrons actively polarizing the nuclei. The Solid Effect (SE) takes place when single electrons polarize their neighboring nuclei [2], the Cross Effect (CE) occurs when pairs of coupled electrons polarize the nuclei [3, 4] and the nuclear polarization enhancement during Thermal Mixing (TM) takes place when spin thermodynamics accounts for the polarization transfer between multi-electron coupled spin systems and the nuclei [5, 6]. All three mechanisms have been used to explain the nuclear enhancement in modern DNP experiments. Modeling of DNP spectra using theoretical models has previously been done mostly relying on the TM-DNP mechanism or by solving coupled rate equations on many electron systems [4] [7] [8] [9] [10] [11]. Many parameters can influence the relative contributions of the three mechanisms to the nuclear signal such as the inhomogeneous linewidth of the electron paramagnetic resonance (EPR) spectrum of the radicals, the hyperfine and electron-electron and nuclear-nuclear dipolar interaction strengths, the radical concentration, the electron and nuclear spin-lattice and spin-spin relaxation parameters and the nuclear Larmor frequencies [12, 13, 14, 15][16] [17].

Presently, where applications of DNP are concerned, two types of solid state DNP experiments are commonly performed: 1) Dissolution DNP, where the DNP enhancement process takes place at low temperatures in one magnetic field, after which the polarized sample is rapidly dissolved and NMR or MRI data are collected at ambient temperatures in a second higher magnetic field [16] [18]. 2) Magic angle spinning (MAS) DNP, where the DNP enhancement and the NMR detection are performed at a constant temperature and magnetic field on a solid sample rotating at the magic angle [15] [16] [17]. Many dissolution DNP experiments use the soluble trityl OX63 radicals [18, 19], while MAS-DNP usually employs TOTAPOL, a stable nitroxide biradical [20], or other biradicals [21, 22, 23, 24]. It has been shown that when using TOTAPOL for MAS DNP the enhancement is considerably higher than when a monoradical such as TEMPOL is used [20]. Consequently other biradicals have been synthesized in recent years and used for different applications [21, 22, 23, 24].

We have recently studied the static DNP enhancement mechanism in the temperature range of 6-40 K in glass forming solids containing TEMPOL [25] and trityl [26] radicals at 3.5 T and detecting ^{1}H and ^{13}C NMR signals, respectively. We found that frequency swept DNP spectra could be decomposed in terms of two basic SE-DNP and CE-DNP lineshapes. This decomposition relied on the assumption that the SE-DNP and CE-DNP mechanisms are simultaneously present and that the components of the DNP enhancement are proportional to the number of MW irradiated SE-DNP active single electrons and CE-DNP active electron pairs in the samples. In both types of samples the presence of the SE was found to be more pronounced at the low temperature range, 6-10 K, than in the higher range, 20-60 K, where the CE seems to dominate. Here we continue our studies by following the DNP enhancement mechanism in samples containing the biradical TOTAPOL in order to examine the influence of its strong electron dipolar coupling (~23 MHz [27]) on the interplay between the relative CE and SE contributions. The presence of these electron pairs would suggest that the CE dominates the

static DNP mechanism [28] [29]. We show here that during our static (non MAS) DNP experiments there is a prominent contribution of the SE-DNP mechanism at the low temperature range. This indicates that the strong electron dipolar interaction is not sufficient to induce CE processes as long as the CE-condition is not fulfilled. The CE condition depends on the g-tensor orientations of the two coupled unpaired electrons in the external magnetic field and thus reduces the number of MW saturated CE-DNP active biradicals. Accordingly, despite the strong dipolar interaction of the electron pairs in the TOTAPOL samples the results of the SE and CE analysis are very similar to the results obtained from the monoradicals TEMPOL and trityl, showing no specific preference for the CE-DNP mechanism. This is in contrast to MAS DNP where level anti-crossings during sample rotation enhance the CE-DNP process, as has been demonstrated in simulations [30, 31]. These anti-crossings have been recently demonstrated experimentally by Corzilius et al. [32]. Additionally we studied the temporal behavior of the DNP enhancement and observed that at low temperatures the growth of the DNP spectra are characterized by two time constants, associated with the individual SE and CE contributions.

2 Methods and materials

2.1 The spectrometer

All experiments were carried out in a hybrid pulsed-EPR-NMR spectrometer at a magnetic field of 3.38 T, which corresponds to a ^{1}H-Larmor frequency of 144 MHz and an electron-Larmor frequency of approximately 95 GHz. The characteristics of the spectrometer were described earlier [33]. Synchronization between the EPR and NMR spectrometers allows independent and simultaneous RF and MW irradiation schemes. There are two MW channels that can be operated independently. A liquid helium flow cryostat positioned inside the magnet enables variable temperature measurements.

2.2 Sample preparation

The experiments were performed on two samples containing 20 mM and 5mM of the nitroxide-based biradical [1-(TEMPO-4-oxy)-3-(TEMPO-4-amino)propan-2-ol] (TOTAPOL) dissolved in a glass forming solution of 56/44 (% w/w) of Dimethyl sulfoxide (DMSO)/H_2O. DMSO was purchased from Sigma-Aldrich and TOTAPOL was purchased from DyNuPol Inc. Thirty μL of the solution were placed in a glass vial, flash frozen with liquid nitrogen and then sealed with a flame. Before sealing the samples were degassed using a freeze-pump-thaw procedure.

2.3 EPR experiments

All EPR signals were detected using an echo detection scheme (α-τ-α-τ-echo) composed of two 400 nsec MW pulses ($\alpha \approx 90^0$) and an echo delay time of τ =600 nsec. In all cases the strength of the MW irradiation was approximately $\omega_1 \approx 600$ kHz as measured from electron nutation

experiments (not shown). The integrated half width echo intensity was recorded for all EPR experiments.

Electron spin-lattice relaxation times, T_{1e}, were measured by saturation-recovery experiments with a MW saturation pulse varying between 10 msec and 150 msec depending on the T_{1e} value. A single exponential fitting procedure was used to analyze the EPR saturation-recovery data:

$$S^e(t) = S^e_{eq} + (S^e(0) - S^e_{eq})exp(-(t/T_{1e})). \quad (1)$$

The T_{1e} values were measured at MW frequencies, ω_{MW} = 94.85 GHz, ω_{MW} = 95 GHz and ω_{MW} = 95.1 GHz and a fixed magnetic field 3.3836 T.

The cw-EPR spectra were measured on a w-band EPR spectrometer in cw-mode, at 10 K, with a modulation amplitude of approximately 1 G, a modulation frequency of 10 kHz, a time constant of 100 msec and sensitivity of 500 μV/pA.

2.4 NMR experiments

All ^{1}H-NMR signals were detected using an echo sequence ($\pi/2_x$-τ-$\pi/2_y$-τ-echo), with a $\pi/2$ pulse of a length of 3 μs and an echo delay of $\tau = 23\,\mu s$. Signals were recorded by acquiring whole echoes and recording their maximum intensity. Integration of the echos resulted in similar results (not shown). The proton longitudinal relaxation times, T_{1n} were measured by saturation recovery. Saturation was achieved by applying a train of 20 alternating x and y saturation pulses. In all cases the resulting signal recovery curves could be analyzed using a single exponent.

2.5 DNP experiments

The DNP experiments were all conducted as follows: A train of proton saturation pulses was applied, followed by continuous wave (cw) MW irradiation at a frequency ω_{MW} applied for a length of time t_{MW} and then NMR echo detection on protons. In all cases the strength of the MW irradiation was approximately $\omega_1 \approx 600$ kHz.

The proton signal enhancements detected at a temperature T for a certain ω_{MW} and t_{MW} were determined by comparing the intensity S_{DNP} of the DNP enhanced ^{1}H echo with the thermal equilibrium echo intensity S_{eq} measured without MW irradiation at the same temperature, according to:

$$E(t_{MW}, \omega_{MW}) = S_{DNP}(t_{MW}, \omega_{MW})/S_{eq}. \quad (2)$$

Temperature dependent DNP enhancements $E(t_{MW}, \omega_{MW})$ were measured as a function of ω_{MW} and t_{MW}, where ω_{MW} was varied between 94.44 GHz and 95.42 GHz, covering the EPR spectral range and beyond. At each temperature at least seven t_{MW} dependent DNP spectra were recorded, starting at t_{MW}=0.1 sec and ending with a t_{MW} which was long enough to allow the enhancement to reach its steady state value. From these data frequency dependent DNP buildup curves were constructed. The buildup curves at fixed tempera-

tures and frequencies were analyzed by fitting them to a single exponential function with a characteristic buildup time $T_{bu}(\omega_{MW})$ and a final maximum steady state enhancement value $E_{max}(\omega_{MW}) = S(5T_{bu}, \omega_{MW})/S_{eq}$:

$$E(t_{MW}, \omega_{MW}) = E_{max}(\omega_{MW})(1 - e^{-t_{MW}/T_{bu}(\omega_{MW})}). \quad (3)$$

3 Experimental results

As a first step towards characterization of the static solid state DNP properties of TOTAPOL, the EPR spectra of the 20 mM (Fig. 1a) and the 5 mM sample (Fig. 1b) were measured at 10 K on a W-band EPR spectrometer in its continuous wave (cw) mode. The differences in the relative intensities of the g_{xx} and g_{yy} components of these cw-EPR spectra are likely a result of broadening effects due to increasing Heisenberg exchange interactions in the more concentrated sample [34].

Next we measured T_{1e} and T_{1n} of the samples as a function of temperature. In Fig. 2a we present the temperature dependence of T_{1e} of the two samples, measured at three frequencies within the EPR powder pattern (see small arrows in Fig. 1); their temperature dependencies turned out to be practically the same. Above 20 K the T_{1e} values are short, of the order of only several msec, and they increase significantly when lowering the temperature, reaching 65 msec at 10 K and 136 msec at 6 K for the 5 mM and the 20 mM samples respectively. As can be seen in Fig. 2b, at high temperatures T_{1n} is several seconds long and as the temperature decreases it increases, reaching a value of 125 sec at 6 K for the 20 mM sample and 339 sec at 10 K for the 5 mM sample.

In Fig. 3 we show the steady state ω_{MW} frequency swept DNP spectra of the two samples measured at $t_{MW} \cong 5T_{bu}$ and at different temperatures. The vertical dashed lines in the figures represent the edges of the EPR spectrum of TOTAPOL as marked by dashed lines in Fig. 1. The first thing to note about that steady state spectra in Fig. 3 is that the enhancements are similar to those observed earlier for TEMPOL, namely the presence of well defined electron spin pairs do not make a significant difference in static DNP. Moreover the maximal enhancement changes as a function of temperature, reaching a maximum at 20 K for the 20 mM sample and 10-20 K for the 5 mM sample. Next we see changes in the DNP spectrum lineshape as a function of temperature that are more pronounced in the 20 mM than in the 5 mM sample. For the 20 mM sample the separation between the maximum positive and negative enhancement peaks is ~305 MHz at 6 K and decreases to ~205 MHz at higher temperatures. The DNP spectra also become narrower as the temperature is increased. The 20 mM spectra at 6 K and 10 K clearly show features of the EPR spectrum such as the ^{14}N steps on the low frequency side. Another feature, a shoulder corresponding to the the g_{xx} part of the EPR line, is seen on the high frequency side on both samples, and it decreases as the temperature increases. Similar effects were previously seen in the spectra of the TEMPOL samples [25], suggesting that also in the TOTAPOL samples we see a transition from a dominant CE mechanism at

high temperatures to a SE mechanism at low temperatures. The analysis of these steady state DNP spectra will be described in the next section.

To investigate the ω_{MW} dependence of the buildup times $T_{bu}(\omega_{MW})$, DNP spectra were recorded as a function of t_{MW} at several temperatures. The DNP spectra at different t_{MW} values are shown in the SI. In Figs. 4a,b the normalized DNP spectra for short and long t_{MW} values, recorded at 6 K and 10 K for the 20 mM and 5 mM samples respectively, are superimposed to demonstrate the changes in their lineshapes. In order to characterize these spectra we monitored the t_{MW} dependence of $E_{DNP}(t_{MW}, \omega_{MW})$ at fixed ω_{MW} values and analyzed the results by assuming that they can be fit to single exponent increasing functions defined by buildup times $T_{bu}(\omega_{MW})$. Their values are shown in Figs. 4c,d (symbols). At low temperatures the MW frequency dependence is very pronounced, with longer $T_{bu}(\omega_{MW})$ values at the center frequency of the DNP spectra than at the sides. At higher temperatures this dependence disappears and the $T_{bu}(\omega_{MW})$ values approach the values of T_{1n}. In both samples some frequency dependence of $T_{bu}(\omega_{MW})$ is still observable at 20 K, while none above that temperature. Several studies have been reported showing frequency dependencies of DNP buildup times. For example, ^{13}C-DNP experiments at ~3.35 T and close to 1 K on samples containing trityl [19], trityl biradicals [35] and TEMPO [9] showed that $T_{bu}(\omega_{MW})$ was shorter in the middle of the DNP spectrum than at the edges. These findings are in contrast to what we show in Fig. 4, though it is difficult to compare as the detected nuclei, the temperature, and in some cases the radical, are different. In the next section we will show that we are able to reproduce the $T_{bu}(\omega_{MW})$ frequency dependence quite well by following the analysis of the DNP spectra as a function of t_{MW}.

4 Analysis of the DNP spectra

In this section we analyze the shapes of the DNP spectra shown in Fig. 3 by decomposing them into two, SE-DNP and CE-DNP, lineshapes, varying their relative contributions (amplitudes) with temperature. These basic SE-DNP and CE-DNP spectra were generated by simulating the steady state nuclear enhancement of a 3-spin system {e-e-H} as a function of the Larmor frequencies of the two electrons and then separating this enhancement profile into a SE and a CE contribution while taking the experimental EPR lineshape into account. A detailed description of this method can be found in reference [25] and in the supplementary material of reference [26].

4.1 The basic SE-DNP and CE-DNP spectra

In the present study we followed the same procedure for the analysis of the DNP spectra as described above. Thus for each sample two basic spectra had to be calculated that can be used to fit all temperature and time dependent DNP spectra data in a way that can then also explain the frequency dependence of the buildup times in Fig. 4c and d (circles). Basic SE-DNP and CE-DNP spectra were indeed calculated based on the cw-EPR lineshapes of Fig.

1 and a best fit procedure was applied to reconstruct the steady state DNP spectra of Fig. 3 for all temperatures. The quality of these fits was somewhat lower than similar fits previously reported [25, 26], especially at low temperatures (see Fig. S1). Moreover it was hard to obtain good fits for the time dependent spectra for short MW irradiation times at these temperatures. Therefore, in order to improve our fitting we slightly modified the lineshapes of the basic SE-DNP spectra used to fit the DNP spectra.

To demonstrate the need for the lineshape modification, we compare in Fig. 5 the experimental DNP spectra of the 20 mM sample measured at 6 K and at $t_{MW} = 0.2$ sec and of the 5mM sample measured at 10 K and $t_{MW} = 0.1$ sec with the simulated basic SE-DNP spectrum (dashed lines). The parameters used for these simulations are listed in the figure caption. The experimental spectra differ from the basic SE-DNP spectrum, having the same overall width and only deviating in their intensity profiles. Most of the intensity differences occur at the edge or outside the EPR lineshape. We therefore decided to modify the basic SE-DNP lineshapes in a way that would result in good fits to the experimental spectra in Fig 5. We did not find it necessary to modify the original CE-DNP lineshape. For the 20 mM sample we choose the modified SE-DNP spectrum to be equal to the experimental spectrum (solid line). For the 5 mM sample we created a modified SE-DNP spectrum (dash-dotted line) that differs slightly from the experimental one by assuming that part of the experimental spectrum is due to CE-DNP and subtracting it from the experimental spectrum to get the modified SE-DNP spectrum. The sum of the modified SE-DNP spectrum (dash-dotten line) and the original basic CE-DNP spectrum (dotted line), with relative amplitudes $b_{SE} : b_{CE} = 84 : 16$, exactly results in the experimental spectrum (solid line). These modified DNP spectra improved the quality of the decomposition significantly for all data, as function of temperature and MW irradiation time for both samples. In addition they enabled us to reconstruct the frequency dependent buildup curves in Fig. 4 c and d, as will be shown in the next section.

To justify the use of these modified lineshapes we should note that the simulated SE-DNP spectra are derived considering only a very small model spin system with representative hyperfine parameters, not taking into account any of the characteristic features of the samples themselves. These include the type of radicals or biradicals, their molecular conformations and concentrations, the molecular composition of the glassy samples influencing the nuclear spin diffusion mechanism and the electron spectral diffusion process causing a frequency dependent saturation of the electron polarization [36] [37]. It could also be that the small amplitude changes were needed as a consequence of the two-electron correlated g-tensor distribution in the biradical samples or as a consequence of the variation of the SE condition width due to different e-e dipolar interactions along the EPR spectrum. The DNP profiles do take into account the influence of the ^{14}N nuclei on the EPR lineshape [25] but not their spin relaxation parameters.

In a previous publication we presented the temperature dependence of the DNP spectra of a degassed 40 mM TEMPOL sample [25]. In that case we did not measure DNP spectra as a function of t_{MW}, but only at the steady state, and the simulated SE-DNP shape resulted in

good fits at all temperatures. Our previous analysis of this sample indicated that at 6 K the DNP spectrum was mainly determined by the SE-lineshape. For comparison purposes in the present study two new TEMPOL DNP spectra were recorded at 6 K, one at $t_{MW} = 0.2$ sec and one at the steady state with $t_{MW} = 240$ sec (see Fig. S10). Both spectra show very similar shapes that again can be analyzed by the basic non-modified DNP spectra. From these fits we can conclude that for TEMPOL at 6 K and above there is no need to modify the basic SE-DNP shape. Whether modifications are necessary below 6 K has to be seen. The difference between the TEMPOL and TOTAPOL SE-lineshapes could be a result of the difference between the unpaired electron distributions in the two corresponding samples, pairs vs monomers. This, however, is a subject that should be verified in the future.

4.2 Steady state and buildup times of the DNP spectra

Using the normalized simulated SE and modified CE lineshapes, $F_{SE}(\omega_{MW})$ and $F_{CE}(\omega_{MW})$, we were able to analyze all experimental DNP enhancement data $E(t_{MW}, \omega_{MW})$ of both samples by fitting them to the function

$$E_{sim}(T; t_{MW}, \omega_{MW}) = b_{SE}(T; t_{MW})F_{SE}(\omega_{MW}) + b_{CE}(T; t_{MW})F_{CE}(\omega_{MW}), \quad (4)$$

where $b_{SE}(T; t_{MW})$ and $b_{CE}(T; t_{MW})$ are the time dependent contributions of the two mechanisms to the enhancements. At the steady state the enhancement profiles $E^{max}_{sim}(T; \omega_{MW})$ are determined by $b^{max}_{SE}(T)F_{SE}(\omega_{MW}) + b^{max}_{CE}(T)F_{CE}(\omega_{MW})$ and the results of the fitting procedures for the 20 mM sample and the 5 mM sample are shown in Fig. 6-7. Summarizing these data the values of $b^{max}_{SE}(T)F_{SE}(\omega_{MW})$ and $b^{max}_{CE}(T)F_{CE}(\omega_{MW})$ at $\nu_{MW} = 94.889$ GHz are shown in Fig. 8. These temperature dependent SE and CE contributions are very similar to the dependencies obtained from the TEMPOL and trityl samples [25, 26].

The results of the fitting procedure as a function of t_{MW} are shown in the SI. In all cases the fits are rather good with only some small mismatches. The resulting amplitude functions $b_{SE}(T; t_{MW})$ and $b_{CE}(T; t_{MW})$ for each temperature could all be described by single exponential functions with buildup times T^{SE}_{bu} and T^{CE}_{bu} and steady state values $b^{max}_{SE}(T)$ and $b^{max}_{CE}(T)$, respectively. Two typical examples of the time dependence of $b_{SE}(T; t_{MW})F_{SE}(\omega_{MW})$ and $b_{CE}(T; t_{MW})F_{CE}(\omega_{MW})$ at $\omega_{MW} = 94.889$ GHz are shown in Fig. 9 along with the SE and CE buildup times as a function of temperature.

Interestingly, the analysis of the DNP data demonstrates that the individual buildup times of the SE and CE contributions differ (Fig. 9). This is most pronounced at low temperatures where $T^{SE}_{bu} < T^{CE}_{bu}$. Comparing these buildup times with T_{1n} shows that for both samples at all temperatures T^{CE}_{bu} is much closer to T_{1n} than T^{SE}_{bu}. The individual buildup times and maximum amplitudes can now be used to express the frequency dependent buildup curves as

$$E_{sim}(T; t_{MW}, \omega_{MW}) = b^{max}_{SE}(T)(1-e^{-t_{MW}/T^{SE}_{bu}(T)})F_{SE}(\omega_{MW}) + b^{max}_{CE}(T)(1-e^{-t_{MW}/T^{CE}_{bu}(T)})F_{CE}(\omega_{MW}) \quad (5)$$

Fitting $E_{sim}(T; t_{MW}, \omega_{MW})$ of each sample to a single exponential function results in frequency

dependent buildup times $T_{bu}^{sim}(T;\omega_{MW})$ that must resemble the experimental buildup times $T_{bu}(T;\omega_{MW})$ as shown in Figs. 3c and d. To reach this resemblance it was necessary to decompose the short time DNP spectra of the 5mM sample (in Fig. 4b) to a (modified) SE-DNP and a CE-DNP contribution, as described above. The frequency dependent buildup curves for the 5 mM sample at 10 K could not be reproduced assuming that the spectrum at $t_{MW} = 0.1$ sec did not contain any CE contribution. The results of these fitting procedures are added to the data in Fig. 4 (solid lines). Although not perfect, the agreement must be considered as a validation of the decomposition of the experimental data in terms of the modified SE-DNP and basic CE-DNP spectra.

5 Discussion

5.1 The DNP spectra

In the present study all DNP spectra could be fit to a sum of two basic SE and CE spectra with different amplitudes $b_{SE}(T;t_{MW})$ and $b_{CE}(T;t_{MW})$, respectively. The difference between their t_{MW} dependencies, expressed by the difference between their buildup times $T_{bu}^{SE}(T)$ and $T_{bu}^{CE}(T)$ at low temperatures, is particularly interesting. These differences and the temperature dependence of the two amplitudes can assist us in getting a better understanding of the DNP mechanisms in our samples. In particular we can try to address the questions what causes the SE and CE buildup times to be different (Fig. 9c-d), and why do the steady state values $b_{SE}^{max}(T)$ and $b_{CE}^{max}(T)$ show different temperature dependencies (Fig. 8)?

We should mention here that the contributions to the polarization coming from the SE provide significant signal enhancements when the MW field is applied outside the EPR line where the CE is absent, thus allowing us to clearly distinguish the SE contribution from the CE one and to characterize them independently. The observed difference between the characteristic buildup times $T_{bu}^{SE}(T)$ and $T_{bu}^{CE}(T)$ suggests that the two enhancement processes operate simultaneously and independently in the whole sample and the differences in $b_{SE}^{max}(T)$ and $b_{CE}^{max}(T)$ suggest that when lowering the temperature the SE contribution to the overall nuclear signal increases.

5.2 The SE-DNP mechanism

To present at least a qualitative explanation for the SE temperature dependence we can imagine a single SE-DNP active electron surrounded by an area filled with nuclei. In such a model we ignore the presence of electrons that are not directly involved in the SE process [38] or are influenced by spectral diffusion [37]. This can be justified by the fact that the shape of the SE-DNP spectrum is almost solely determined by the density of single electrons with on-resonance DQ and ZQ transitions at each MW frequency. We also neglect the biradical nature of TOTAPOL which can be justified by realizing that in most cases the frequencies of the DQ (or ZQ) transitions of the two electrons will be very different. The description of the SE-DNP process we will present here relies on earlier studies which describe nuclear spin diffusion [39]

[40] [41] [42] and the SE-DNP mechanism [6] [43] [44], and in particular the SE description presented by Hovav et al. [12] [45].

To schematically demonstrate the effects of different experimental and intrinsic parameters of the system on the nuclear polarization we introduce a simple model of a two-dimensional grid of nuclei surrounding a single electron. To calculate the effect of MW irradiation at $\omega_e - \omega_n$ (or $\omega_e + \omega_n$) on the different nuclei we assign to each nucleus i an effective DQ (or ZQ) irradiation field $\omega_{eff,i}^{SE}$, which is proportional to the strength ω_1 of the MW and inversely proportional to the cube of the electron-nuclear distance [12]. The nuclear dipolar interaction is taken into account by slightly modifying $\omega_{eff,i}^{SE}$ in order to support the dipolar-assisted DNP enhancement mechanism [45]. The modification is done by spreading $\omega_{eff,i}^{SE}$ to the nuclei j around it. The exact way this has been done here is discussed in the SI.

With the corrected irradiation fields, $\omega_{1,eff,i}^{SE*}$, we can now describe the evolution of polarizations of the nuclei i by introducing rate equations for all polarizations in the system with DNP excitation rate constants $R_{bu,i}^{SE} = (\omega_{eff,i}^{SE*})^2 T_{2x}$, which depend on the e-n spin-spin cross-relaxation time T_{2x}. The electronic relaxation rate R_{1e} in these equations is chosen much larger than all $R_{bu,i}^{SE}$'s and as a result does not influence the buildup time of the individual nuclear polarizations [12]. For nuclei close to the electron (i.e. the core nuclei according to reference [12]) the relaxation rate R_{1c} is assumed to be larger than the relaxation rate R_{1n} of the rest of the nuclei, and is chosen here to be $R_{1c} = 10 \cdot R_{1n}$. The spin diffusion process, represented by a dipolar relaxation rate R_{1d} in the equations (see SI), equalizes the polarization of neighboring nuclei [39] [42] [46]. The quenching of the nuclear dipolar interaction by the electron-nuclear hyperfine interaction is taken into account by using a spin diffusion rate R_{1d}^{c} between the core nuclei that is 100 times smaller than the main R_{1d} value. In all cases $R_{1d} \gg R_{1n}$ such that the bulk polarization is mostly uniform. The model system and the rate equations used to evaluate the individual polarizations are described in detail in the SI.

In the following figures we show results of calculations of the DNP enhanced nuclear polarization on such two dimensional grids. The electron (represented by the black pixel) is located close to the lower left corner and the color of each additional pixel represents the magnitude of the polarization of each nucleus, normalized to the electron steady state polarization.

In Fig. 10a we show the steady state nuclear polarizations of the system containing $N_{SE} = 1680$ nuclei during MW irradiation for a nuclear relaxation rate of $R_{1n} = 0.01 sec^{-1}$ and a spin diffusion rate $R_{1d} = 0$. In this case only direct polarization of the nuclei through the effective irradiation $\omega_{eff,i}^{SE*}$ is possible. As a result the polarization is localized in an area around the electron.

In Fig 10b we show the nuclear polarization when choosing $R_{1d} = 10^3 sec^{-1}$. Comparing (a) and (b) demonstrates the effect of R_{1d} spreading the polarization uniformly and destroying the localization. To show an example of the dependence on R_{1n} we recalculated the polarization in Fig. 10c by increasing R_{1n} to $0.2\, sec^{-1}$. All other parameters such as the distances between the nuclei and the R_{1e}, R_{1c} and R_{1d}^{c} values are given in the figure caption. (An example of nuclei polarized by two electrons is discussed and demonstrated in the SI). As long as R_{1d} is much larger

than R_{1n} our simulations show that all nuclei (except for part of the core nuclei) experience about the same polarization buildup rate R_{bu}^{SE} and reach about the same end polarization P_{end}^{SE}. The values of P_{end}^{SE} and R_{bu}^{SE} are of course a function of the $R_{bu,i}^{SE}$'s, of R_{1e}, R_{1n}, R_{1c} and of the number of nuclei N_n^{SE} in the model [6, 43]. A qualitative description of this dependence is given below.

In the absence of nuclear relaxation, $R_{1n} \approx 0$ and for a large R_{1e}, the buildup rate of the nuclei $R_{bu}^{SE,0}$ is mainly determined by the strength of the MW irradiation, the number, N_n^{SE}, of nuclei around the electron and their geometry [45]. In the presence of nuclear relaxation, $R_{1n} \neq 0$, the buildup rate decreases depending on the actual values of R_{1n} and N_n^{SE}. For increasing R_{1n} or N_n^{SE} the value of R_{bu}^{SE} will approach R_{1n} and will eventually become equal to it. For which values of R_{1n} this happens depends of course on the value of $R_{bu}^{SE,0}$ and thus on ω_1. The actual dependence on R_{1n} and N_n^{SE} is hard to predict and is outside the scope of our present qualitative description.

In addition to the changes in the buildup rate, the end polarization P_{end}^{SE} is also a function of R_{1n} and N_n^{SE}. For $R_{1n} = R_{1c} = 0$ the value of P_{end}^{SE} will be about equal to the initial electron polarization, independent of N_n^{SE} as long as R_{1d} is really large. When $R_{1c} > 0$ P_{end}^{SE} will decrease even when $R_{1n} = 0$. For a constant R_{1c} the P_{end}^{SE} value will decrease for increasing R_{1n} and N_n^{SE} values and can reach zero when R_{1n} is sufficiently large. Furthermore, the larger the $R_{bu,i}^{SE}$'s the more nuclei can be polarized before P_{end}^{SE} reaches zero. An example of the dependence of R_{bu}^{SE} and P_{end}^{SE} on R_{1n} for our model is shown in Fig. 11 for different N_n^{SE} values going again from 440 to 5040 nuclei.

Following the results of these model calculations and the discussions on the spin diffusion process in the literature [6] [12] [39] [42] [43] [44] [46] we can determine which of the parameters R_{1e}, R_{1n}, $R_{bu}^{SE,0}$, and N_n^{SE} influences the SE enhancement in the samples studied. Here N_n^{SE} is a parameter representing the average number of nuclei that are polarized by each SE-DNP active electron. The small SE contribution at high temperatures can be attributed to the large R_{1n} causing P_{end}^{SE} to approach zero and R_{bu}^{SE} to become equal to R_{1n}. At the low temperatures R_{1n} becomes small enough to increase P_{end}^{SE} and make $R_{bu}^{SE} > R_{1n}$, as observed experimentally and as predicted in other model calculations [6] [11] [12] [43] [47]. The magnitude of N_n^{SE} is determined by the density of the DNP active electrons and will increase going from 20mM to the 5 mM sample. For the 20 mM sample $R_{1n} = 0.063\,sec^{-1}$ at 40K and becomes $R_{1n} = 0.007\,sec^{-1}$ at 6 K, causing an increase in P_{end}^{SE}. Similar effects are seen for the 5 mM sample. Additionally, the ~5 fold growth of R_{1n} at 10 K going from the 5mM ($R_{1n} = 0.003\,sec^{-1}$) to the 20 mM ($R_{1n} = 0.014\,sec^{-1}$) sample could explain the low value of the SE enhancement (P_{end}^{SE}) in the 20 mM sample with respect to the 5 mM sample. This is qualitatively consistent with the SE results in Fig. 8. We must emphasize that the influence of R_{1e} on our SE-DNP results is expected to be minor, because at 6 K its maximum value $R_{1e} = 65\,sec^{-1}$ is still much larger than $R_{bu}^{SE} = T_{bu}^{SE}(6)^{-1} = 0.024\,sec^{-1}$.

This discussion provides a possible answer to the question why the SE enhancement disappears at high temperatures. The decay of the SE enhancement with temperature occurs of

course gradually, resulting in a coexistence of the two processes in the sample in the intermediate range of temperatures.

5.3 The CE-DNP mechanism

At the high temperature range of our experiments the CE-DNP process seems to dominate. This can either be due to the absence of the SE-DNP enhancement (see above) or that when both processes are present the CE-DNP process dominates. Thus we have to verify why the conditions suppressing SE-DNP do not do the same to the CE-DNP process. To answer this we can rely on the above discussion about the SE case. The main reason for the absence of the SE enhancement was the large R_{1n} values and insufficient effective MW fields. We must therefore show that for these R_{1n}'s and the same ω_1 the CE-DNP enhancement efficiency can be much higher than the SE-DNP efficiency. Since the CE-enhancement relies also on the same spin diffusion process as in the SE case and on the same R_{1n}, the origin of the difference between the processes must come from the polarization of the nuclear spins close to the electrons. This argument is even strengthened by the fact that the density of CE-DNP active electron pairs is smaller than that of the SE-DNP active electrons.

The major part of the electrons are not directly influenced by DQ or ZQ excitation necessary for the SE process or do not belong to CE spin pairs. However, they get partially depolarized by SQ saturation and by spectral diffusion processes possibly inducing DNP enhancement [11] [47] [48]. Because of the low density of CE-DNP active electron pairs, this spectral diffusion assisted enhancement can become rather important for spreading the polarization over the sample. This kind of enhancement is now under investigation and is outside the scope of this article.

When the Larmor frequencies $\omega_{e,1}$ and $\omega_{e,2}$ of two dipolar interacting electrons, 1 and 2, satisfy $|\omega_{e,1} - \omega_{e,2}| \backsimeq \omega_n$, we expect degeneracies between the energies of states of the form $|\alpha_1\beta_2\psi_m^n >$ and $|\beta_1\alpha_2\psi_{m\pm1}^n >$, where the nuclear states $|\psi_m^n >$and $|\psi_{m\pm1}^n >$ differ by a single spin flip of some nucleus i. When these nuclei are hyperfine coupled to the electrons strong state mixing can occur and the MW matrix elements between the states of the form

$$< \alpha_1\alpha_2\psi_m^n|H_{MW}|\frac{1}{\sqrt{2}}[(\alpha_1\beta_2\psi_m^n) \pm (\beta_1\alpha_2\psi_{m\pm1}^n)] > \quad (6)$$

$$< \beta_1\beta 2\psi_m^n|H_{MW}|\frac{1}{\sqrt{2}}[(\alpha_1\beta_2\psi_m^n) \pm (\beta_1\alpha_2\psi_{m\pm1}^n)] > \quad (7)$$

can become of the order of ω_1 itself. These large values, combined with the action of possible cross-relaxation [11] between states of the form $|\alpha_1\beta\psi_m^n >$ and $|\beta_1\alpha_2\psi_{m\pm1}^n >$ due to fluctuations of the high order matrix elements, can result in an enhancement of neighboring nuclei with buildup rates approaching R_{1e} [13]. Thus the effective MW excitation rates $R_{bu,i}^{CE}$ for part of the neighboring nuclei can become much larger than in the SE case. In the absence of nuclear relaxation, $R_{1n} \approx 0$ the buildup rate of the nuclei around the CE electron pairs $R_{bu}^{CE,0}$ is mainly determined by the strength of the MW irradiation, the number of nuclei around the electron,

N_n^{CE}, and their geometry. How much the value of $R_{bu}^{CE,0}$ exceeds $R_{bu}^{SE,0}$ for the same relaxation parameters depends on different factors including the number of nuclei with large $R_{bu,i}^{CE}$ rates. This is still under investigation and we do not have a good model to simulate polarization distributions analogous to Figs. 10 and 11. It is however apparent that the increase of R_{1e} with temperature enlarges $R_{bu}^{CE,0}$ and increases the CE-DNP enhancement efficiency at higher temperatures. Together with the spectral diffusion assisted enhancement, we conclude that the shortening of the electron relaxation time is one of the main reasons for the dominance of the CE lineshapes at high temperatures.

In the MAS DNP case, the CE works in an entirely different manner. The rotation of the sample can result in adiabatic energy level crossings which in turn result in high nuclear polarizations [30] [31]. These energy level crossing are much more probable than finding a pair of electrons at the CE condition in the static case. Additionally, because of the sample rotation the MW irradiation excites many more electrons than in the static case. As a result in MAS DNP the CE is much more efficient than in the static DNP case.

The arguments used in this section provide a qualitative interpretation of our results, but make no predictions about the absolute values of the experimental enhancements or buildup times. For a more accurate description the SE and CE enhancements in large spin systems must be combined and the depolarization of electrons via spectral diffusion [37] [47] [48] must be taken into account.

5.4 Conclusions

This paper presents ^{1}H-DNP results of samples containing 20 mM and 5 mM of the biradical TOTAPOL. By analyzing the steady state DNP spectra we show that in the static (non MAS) case TOTAPOL behaves very similarly to its monoradical analog TEMPOL and gives similar enhancement [25]. Namely, when using TOTAPOL the SE is dominant at low temperatures and decreases at high temperatures where the CE becomes dominant. No increase in the propensity of CE is found despite the strong electron-electron dipolar couplings which result from TOTAPOL being a biradical. We also show that the DNP buildup time is dependent on the MW irradiation frequency. We are able to reproduce this MW frequency dependence by analyzing the DNP spectra as a function of the MW irradiation time. This analysis results in different buildup times for the SE and the CE, especially at low temperatures, where T_{bu}^{SE} is faster than T_{1n} and T_{bu}^{CE} is close to T_{1n}. This temperature behavior of the SE is demonstrated using a rate equation model described. It shows that at low temperatures the long T_{1n} causes an increase in the SE and results in a T_{bu}^{SE} that is shorter than T_{1n}. As the temperature rises T_{1n} becomes shorter, the SE decreases and T_{bu}^{SE} approaches T_{1n}. At the moment we cannot model the CE in a similar manner but we suggest that the large effective irradiation on the CE nuclei and the shortening of T_{1e} at high temperatures results in an increase in CE enhancement when the SE is inefficient. Finally, we observe a change in the lineshape of the SE-DNP spectrum with TOTAPOL when compared to TEMPOL, the exact nature of which is currently not understood though some suggestions were made.

Acknowledgments

We would like to thank Dr. Yonatan Hovav for many helpful discussions on all aspects of this work. We would also like to thank Dr. Andrea Martorana for help with acquiring the cw W-band EPR spectra. The work was supported by the German-Israeli Project Cooperation of the DFG through a special allotment by the Ministry of Education and Research (BMBF) of the Federal Republic of Germany. This research was also made possible in part by the historic generosity of the Harold Perlman Family. S.V. holds the Joseph and Marian Robbins Professorial Chair in Chemistry. D.G. holds the Erich Klieger Professorial Chair in Chemical Physics.

References

[1] A. W. Overhauser, Phys. Rev., 1953, 92, 411.

[2] C. Jefferies, Phys. Rev. 106, (1957), 164

[3] C. F. Hwang and D. A. Hill, Phys. Rev. Lett. 18,(1967), 110

[4] C. F. Hwang and D. A. Hill, Phys. Rev. Lett. 19,(1967), 1011

[5] A. Abragam and M. Borghini, Progress in Low Temperature Physics (North-Holland, Amsterdam, 1964), Vol. 4.

[6] A. Abragam and M. Goldman, Reports on Progress in Physics 41 (1978), 395-467.

[7] W. de Boer, J. Low Temp. Phys., 1976, 22, 185-212.

[8] C. T. Farrar, D. A. Hall, G. J. Gerfen, S. J. Inati and R. G. Griffin, J. Chem. Phys., 2001, 114, 4922-4933.

[9] S. Jannin, A. Comment, F. Kurdzesau, J. A. Konter, P. Hautle, B. van den Brandt and J. J. van der Klink, J. Chem. Phys., 2008, 128, 241102 (DOI:10.1063/1.2951994).

[10] S. Jannin, A. Comment and J. van der Klink, Applied Magnetic Resonance, 2012, 43, 59-68.

[11] S. C. Serra, A. Rosso and F. Tedoldi, Phys. Chem. Chem. Phys., 2013, 15, 8416-8428.

[12] Y. Hovav, A. Feintuch and S. Vega, J. Chem. Phys., 2011, 134, 074509.

[13] Y. Hovav, A. Feintuch and S. Vega, Journal of Magnetic Resonance, 2012, 214, 29-41.

[14] Y. Hovav, A. Feintuch and S. Vega, Physical Chemistry Chemical Physics, 2013, 15, 188-203.

[15] T. Maly, G. T. Debelouchina, V. S. Bajaj, K. Hu, C. Joo, M. L. Mak-Jurkauskas, J. R. Sirigiri, P. C. A. van der Wel, J. Herzfeld, R. J. Temkin and R. G. Griffin, J. Chem. Phys., 2008, 128, 052211.

[16] K. Sze, Q. Wu, H. Tse and G. Zhu, in , ed. ed. G. Zhu, (Springer Berlin Heidelberg, 2012), pp.215-242.

[17] Q. Z. Ni, E. Daviso, T. V. Can, E. Markhasin, S. K. Jawla, T. M. Swager, R. J. Temkin, J. Herzfeld and R. G. Griffin, Acc. Chem. Res., 2013, 46, 1933-1941.

[18] J. H. Ardenkjær-Larsen, B. Fridlund, A. Gram, G. Hansson, L. Hansson, M. H. Lerche, R. Servin, M. Thaning and K. Golman, Proceedings of the National Academy of Sciences, 2003, 100, 10158-10163.

[19] H. Jóhannesson, S. Macholl and J. H. Ardenkjær-Larsen, Journal of Magnetic Resonance, 2009, 197, 167-175.

[20] C. Song, K. Hu, C. Joo, T. M. Swager and R. G. Griffin, J. Am. Chem. Soc., 2006, 128, 11385-11390.

[21] Y. Matsuki, T. Maly, O. Ouari, H. Karoui, F. Le Moigne, E. Rizzato, S. Lyubenova, J. Herzfeld, T. Prisner, P. Tordo and R. Griffin, Angewandte Chemie International Edition, 2009, 48, 4996-5000.

[22] 1 C. Ysacco, H. Karoui, G. Casano, F. Le Moigne, S. Combes, A. Rockenbauer, M. Rosay, W. Maas, O. Ouari and P. Tordo, Applied Magnetic Resonance, 2012, 43, 251-261.

[23] C. Sauvée, M. Rosay, G. Casano, F. Aussenac, R. T. Weber, O. Ouari and P. Tordo, Angewandte Chemie International Edition, 2013, 52, 10858-10861.

[24] A. Zagdoun, G. Casano, O. Ouari, M. Schwarzwalder, A. J. Rossini, F. Aussenac, M. Yulikov, G. Jeschke, C. Coperet, A. Lesage, P. Tordo and L. Emsley, J. Am. Chem. Soc., 2013, 135, 12790-12797.

[25] D. Shimon, Y. Hovav, A. Feintuch, D. Goldfarb and S. Vega, Phys. Chem. Chem. Phys., 2012, 14, 5729-5743.

[26] D. Banerjee, D. Shimon, A. Feintuch, S. Vega and D. Goldfarb, Journal of Magnetic Resonance, 2013, 230, 212-219.

[27] K. Hu, C. Song, H. Yu, T. M. Swager and R. G. Griffin, J. Chem. Phys., 2008, 128, 052302.

[28] K. Hu, G. T. Debelouchina, A. A. Smith and R. G. Griffin, J. Chem. Phys., 2011, 134, 125105.

[29] K. Hu, Solid State Nucl. Magn. Reson., 2011, 40, 31-41.

[30] F. Mentink-Vigier, U. Akbey, Y. Hovav, S. Vega, H. Oschkinat and A. Feintuch, Journal of Magnetic Resonance, 2012, 224, 13-21.

[31] K. R. Thurber and R. Tycko, J. Chem. Phys., 2012, 137.

[32] . Corzilius, L. B. Andreas, A. A. Smith, Q. Z. Ni and R. G. Griffin, Journal of Magnetic Resonance.

[33] A. Feintuch, D. Shimon, Y. Hovav, D. Banerjee, I. Kaminker, Y. Lipkin, K. Zibzener, B. Epel, S. Vega and D. Goldfarb, J. Magn. Reson., 2011, 209, 136-141.

[34] S. Ruthstein, R. Artzi, D. Goldfarb and R. Naaman, Phys. Chem. Chem. Phys., 2005, 7, 524-529.

[35] S. Macholl, H. Johannesson and J. H. Ardenkjær-Larsen, Phys. Chem. Chem. Phys., 2010, 12, 5804-5817.

[36] J. Granwehr and W. Köckenberger, Applied Magnetic Resonance, 2008, 34, 355-378.

[37] K. M. Salikhov, Yu D. Tsvetkov, in Time Domain Electron Spin Resonance. L. Kevan, R.N. Schwartz (Wiley-Interscience, New York 1979).

[38] Y. Hovav, O. Levinkron, A. Feintuch and S. Vega, Applied Magnetic Resonance, 2012, 43, 21-41.

[39] A. E. Dementyev, D. G. Cory and C. Ramanathan, Phys. Rev. B, 2008, 77, 024413.

[40] A. Abragam, Principles of Nuclear Magnetism (Clarendon Press, Oxford, 1961).

[41] M. Afeworki and J. Schaefer, Macromolecules, 1992, 25, 4092-4096.

[42] S. F. J. Cox, S. F. J. Read and W. Th. Wenchebach, Journal of Physics C: Solid State Physics, 1977, 10, 2917.

[43] A. A. Smith, B. Corzilius, A. B. Barnes, T. Maly and R. G. Griffin, J. Chem. Phys., 2012, 136.

[44] O. S. Leifson and C. D. Jeffries, Phys. Rev., 1961, 122, 1781.

[45] Y. Hovav, A. Feintuch and S. Vega, J. Chem. Phys., 2011, 134, 074509

[46] M. Ernst and B. H. Meier, Studies in Physical and Theoretical Chemistry, 84, (Elsevier, 1998) .

[47] D. S. Wollan, Phys. Rev. B, 1976, 13, 3671-3685.

[48] V. A. Atsarkin and A. V. Kessenikh, Applied Magnetic Resonance, 2012, 43, 7-19.

Figure Captions

Fig. 1: cw-EPR spectra of the (a) 20 mM and (b) 5 mM TOTAPOL samples measured at 10K on a W-band EPR spectrometer in its cw mode. The dotted vertical lines represent the edges of the EPR lines. The small arrows represent the frequencies where T_{1e} was measured.

Fig. 2: (a) Electron spin-lattice relaxation times T_{1e} and (b) nuclear spin-lattice relaxation times T_{1n} as a function of temperature measured between 6 K and 40 K. The T_{1e} values of the 20 mM (filled symbols) and 5 mM (empty symbols) measured at $\omega_{MW} = 94.85$ GHz (black circles), $\omega_{MW} = 95$ GHz (magenta circles) and $\omega_{MW} = 95.1$ GHz (blue triangles). The T_{1n} values are plotted for the 20 mM (circles) and 5 mM (squares) samples. Error bars represent the 95% confidence interval of the timescale parameters resultant from the fitting procedure of the electron and nuclear saturation recovery curves. In some cases the error bars are obscured by the symbols. The lines in this figure are to guide the eye.

Fig. 3: Frequency swept DNP spectra $E_{max}(\omega_{MW})$ of the (a) 20 mM and the (b) 5 mM samples measured at 6 K (cyan), 10 K (magenta), 20 K (green), 30 K (blue) and 40 K (red) at $t_{MW} \approx 5T_{bu}$. The dotted vertical lines represent the edges of the EPR line as marked in Fig. 1. The lines in this figure are to guide the eye.

Fig. 4: Low temperature frequency swept DNP spectra $E(t_{MW}, \omega_{MW})$ for short t_{MW} values (circles) and long t_{MW} values (squares) for the (a) 20 mM and (b) the 5 mM samples (b) at 6 K and 10 K respectively. $T_{bu}(\omega_{MW})$ as a function of temperature (filled symbols) for the (c) 20 mM and (d) the 5 mM samples. The T_{1n} value for each temperature is plotted on the edge of figures (c) and (d) in empty symbols. Error bars represent the 95% confidence interval of the timescale parameters resultant from the fitting procedure of the polarization buildup curves. In some cases the error bars are obscured by the symbols. The lines in (a) and (b) are to guide the eye.

Fig. 5: Comparison between the experimental DNP spectra $E(t_{MW}, \omega_{MW})$ (circles) of the (a) 20 mM sample measured at 6 K and at $t_{MW} = 0.2$ ms and of the (b) 5mM sample measured at 10 K and $t_{MW} = 0.1$ ms with the basic calculated SE-DNP spectra (dashed lines). The parameters used for the simulations SE and CE spectra were: $\omega_n/2\pi = 144$ MHz, $\omega_{MW}/2\pi = 95$ GHz, $D_{ab} = D_{ab}^{\pm} = 20$ MHz, $A_{z,an} = 0$ kHz, $A_{an}^{\pm} = 500$ kHz, $A_{z,bn} = 0$ kHz, $A_{bn}^{\pm} = 0$ kHz, $\omega_1/2\pi = 0.5$ MHz, $T_{1e} = 10$ msec, $T_{1c} = 1$ sec, $T_{2e} = 4$ usec, $T_{2n} = 1$ msec, $T = 10$ K. The SE and CE spectra for each sample were simulated using their respective cw-EPR lines.

Fig. 6: Analysis of the frequency swept DNP spectra $E(t_{MW}, \omega_{MW})$ (circles) of the 20 mM sample measured at (a) 6 K, (b) 10 K, (c) 20 K and (d) 40 K at $t_{MW} \approx 5T_{bu}$. Shown are the SE contribution $b_{SE}(t_{MW})F_{SE}(\omega_{MW})$ (magenta lines), the CE contribution $b_{CE}(t_{MW})F_{CE}(\omega_{MW})$ (blue lines) and the fit $S_{sim}(t_{MW}, \omega_{MW})$ (black lines). The fitting procedure is described in the

text.

Fig. 7: Analysis of the frequency swept DNP spectra $E(t_{MW}, \omega_{MW})$ (circles) of the 5 mM sample measured at (a) 10 K, (b) 20 K, (c) 30 K and (d) 40 K at $t_{MW} \approx 5T_{bu}$. Shown are the SE contribution $b_{SE}(t_{MW})F_{SE}(\omega_{MW})$ (magenta lines), the CE contribution $b_{CE}(t_{MW})F_{CE}(\omega_{MW})$ (blue lines) and the fit $S_{sim}(t_{MW}, \omega_{MW})$ (black lines). The fitting procedure is described in the text.

Fig. 8: The contributions of the SE $b_{SE}(t_{MW})F_{SE}(\omega_{MW})$ (circles) and the CE $b_{CE}(t_{MW})F_{CE}(\omega_{MW})$ (squares) to the enhancements derived from Figs. 9-10 as a function of temperature for (a) the 20 mM and (b) the 5 mM samples plotted at $\nu_{MW} = 94.889$ GHz. The lines in this figure are to guide the eye.

Fig. 9: Example of b-functions for the SE: $b_{SE}(t_{MW})F_{SE}(\omega_{MW})$ (circles), CE: $b_{CE}(t_{MW})F_{CE}(\omega_{MW})$ (squares) and the fit: $b_{SE}(t_{MW})F_{SE}(\omega_{MW})+b_{CE}(t_{MW})F_{CE}(\omega_{MW})$ (triangles) plotted at $\nu_{MW} =$ 94.889 GHz for (a) the 20 mM and (b) the 5 mM sample at 6 K and 10 K, respectively. Their single exponential fits are shown as dashed lines. (c)-(d) Plots of T_{bu}^{SE} (circles, solid lines), T_{bu}^{CE} (squares, solid lines) and T_{1n} (triangles, dashed lines) as a function of temperature for (c) the 20 mM and (d) the 5 mM sample. The T_{1n} values are repeated from Fig. 2(b). Error bars in (c) and (d) represent the 95% confidence interval of the timescale parameters resultant from the fitting procedure of the b-functions and nuclear saturation recovery curves with single exponents. In some cases the error bars are obscured by the symbols. The lines in (c) and (d) are to guide the eye.

Fig. 10: 2D contour plots of the steady state nuclear polarization for showing the effect of (a) short R_{1n} and no spin diffusion [$R_{1n} = 10^{-2}\ sec^{-1}$ and $R_{1d} = R_{1d}^{c} = 0\ sec^{-1}$], (b) short R_{1n} and fast spin diffusion [$R_{1n} = 10^{-2}\ sec^{-1}$, $R_{1d} = 10^{3}\ sec^{-1}$ and $R_{1d}^{c} = 10\ sec^{-1}$] and (c) long R_{1n} and fast spin diffusion [$R_{1n} = 2 \cdot 10^{-1}\ sec^{-1}$, $R_{1d} = 10^{3}\ sec^{-1}$ and $R_{1d}^{c} = 10\ sec^{-1}$]. The electron is marked by a black pixel in the lower left corner of each contour plot. Each nucleus is a pixel whose color represents the nuclear polarization normalized to the electron thermal equilibrium polarization. The nuclei are 3.1 A apart in both dimensions, and there are 960 nuclei in all. The other parameters of the system are: $R_{1e} = 10\ sec^{-1}$, $R_{1c} = 10 \cdot R_{1n}\ sec^{-1}$, $\omega_1 = 1$ MHz and $T_{2x} = 5\mu sec$. The rate equations used to calculate these plots are described in detail in the SI.

Fig. 11: P_{end} and R_{bu}^{SE} as a function of R_{1n} for different values of N_n^{SE}, described in the legend. In the lower panel the dotted line represents $R_{bu}^{SE} = R_{1n}$. The parameters used for these calculations are: $R_{1e} = 10\ sec^{-1}$, $R_{1c} = 10 \cdot R_{1n}\ sec^{-1}$, $R_{1d} = 10^{3}\ sec^{-1}$, $R_{1d}^{c} = 10\ sec^{-1}$, $\omega_1 = 1$ MHz and $T_{2x} = 5\mu sec$. The rate equations used to calculate these plots are described in detail in the SI.

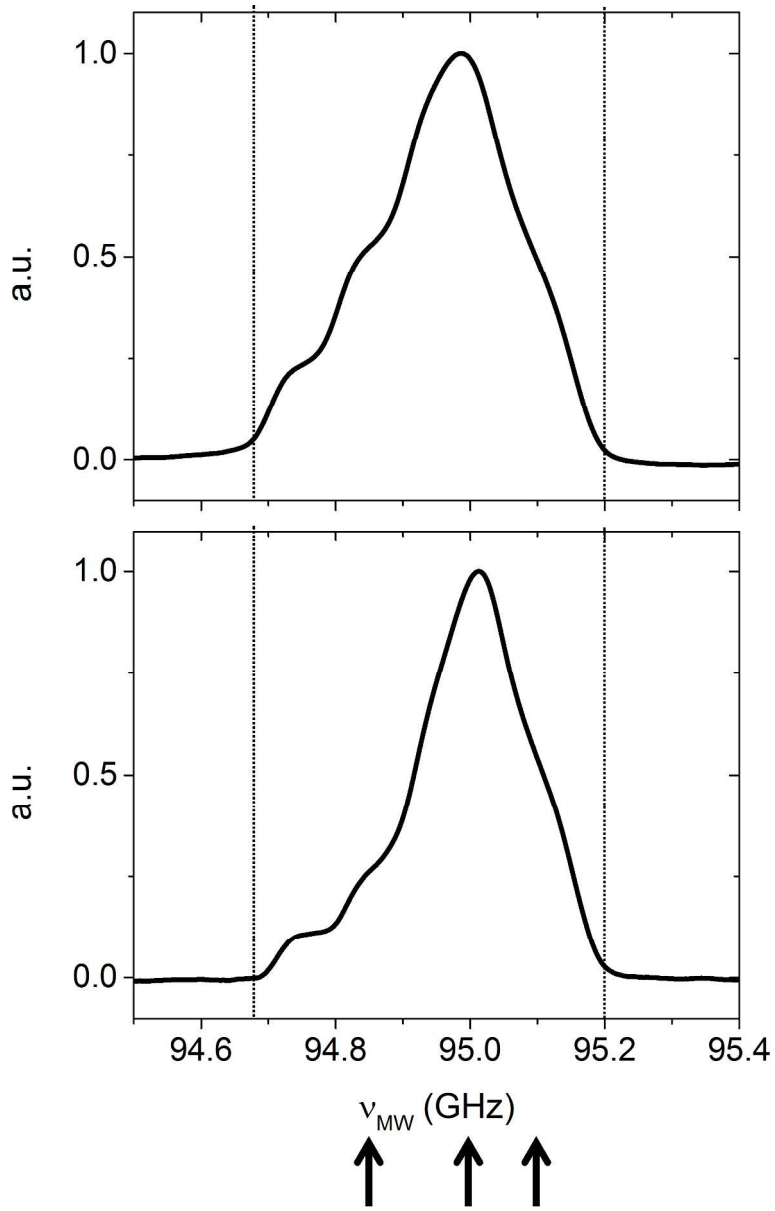

459x728mm (120 x 120 DPI)

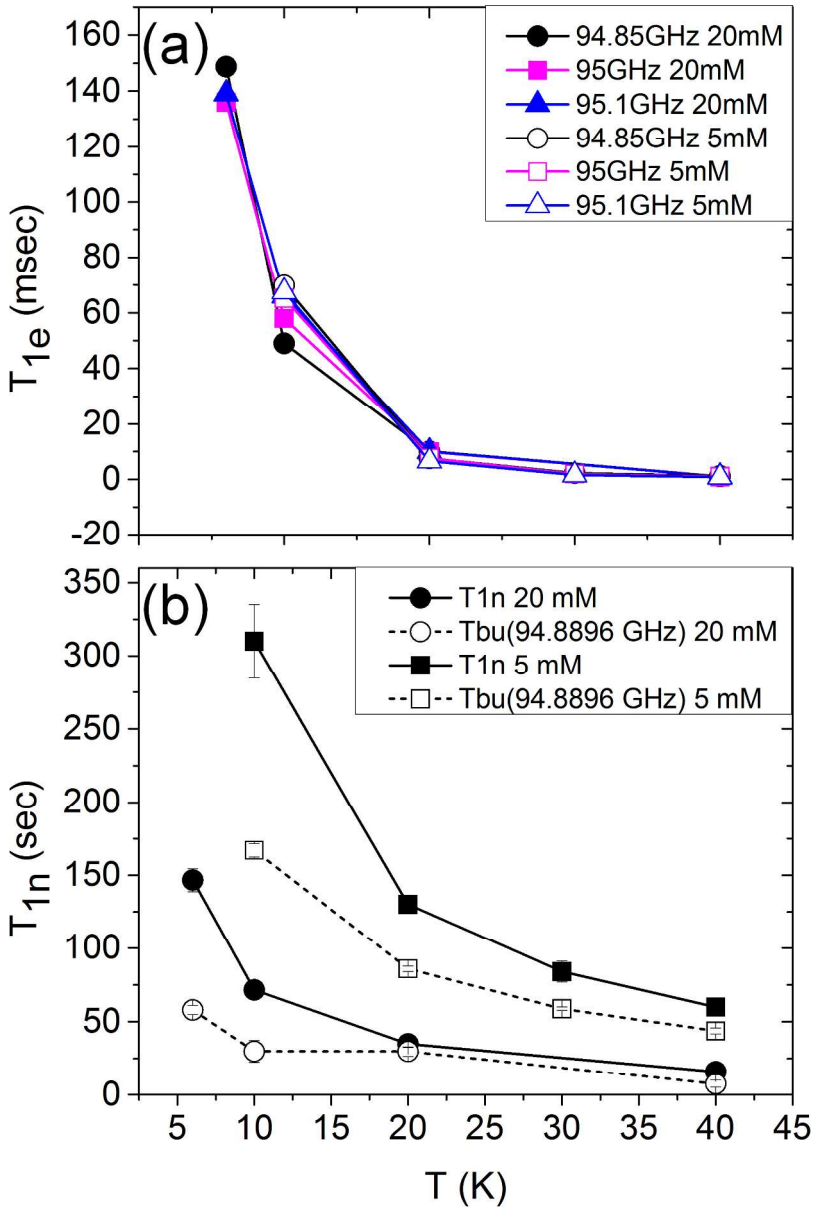

450x674mm (120 x 120 DPI)

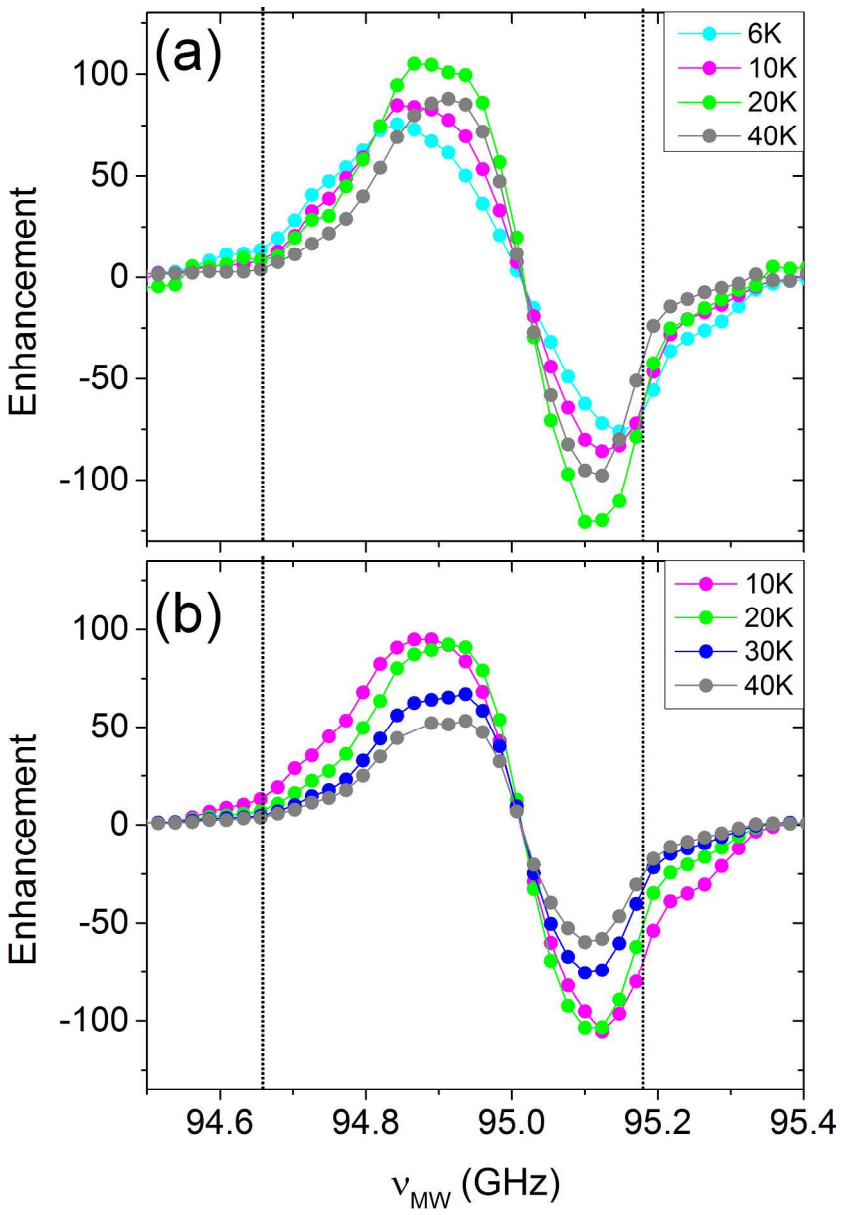

463x672mm (120 x 120 DPI)

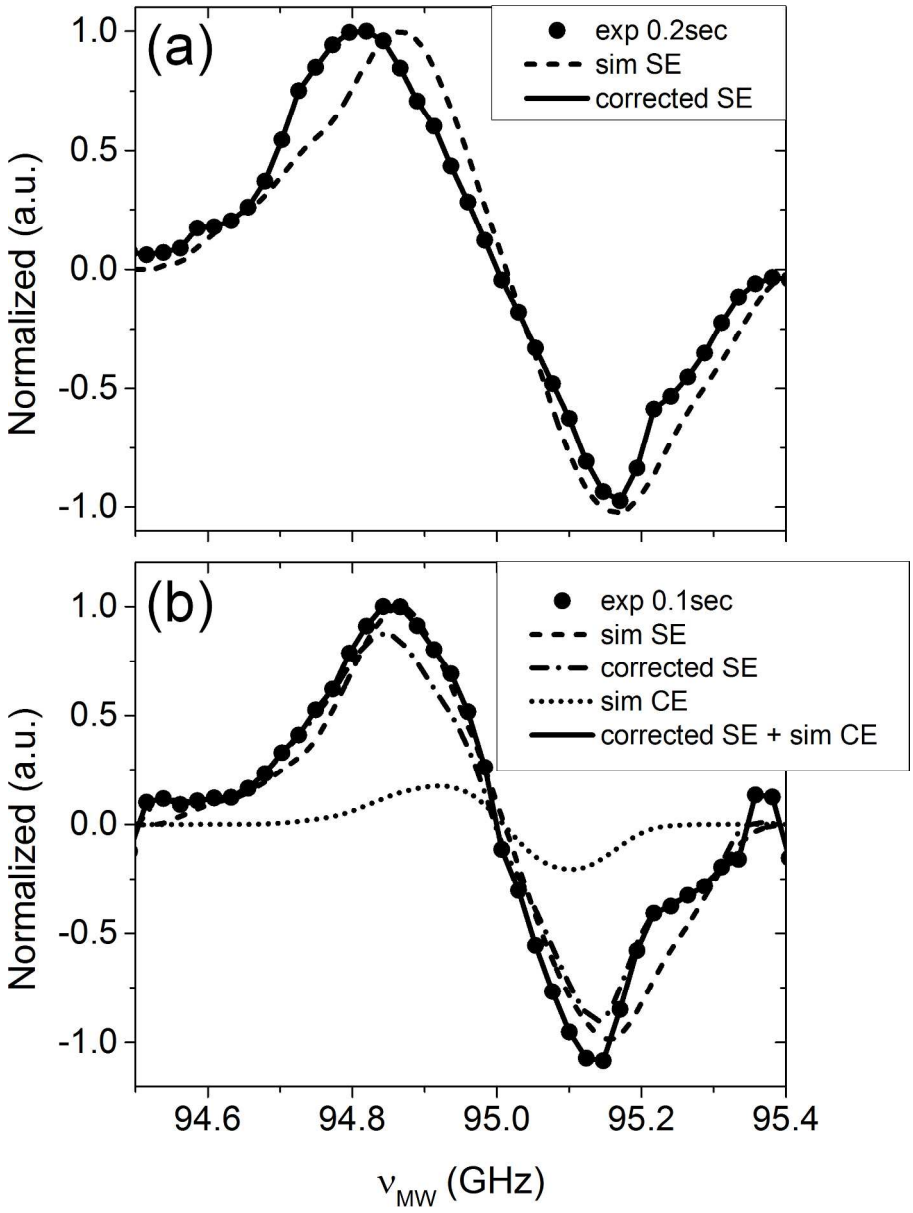

509x679mm (120 x 120 DPI)

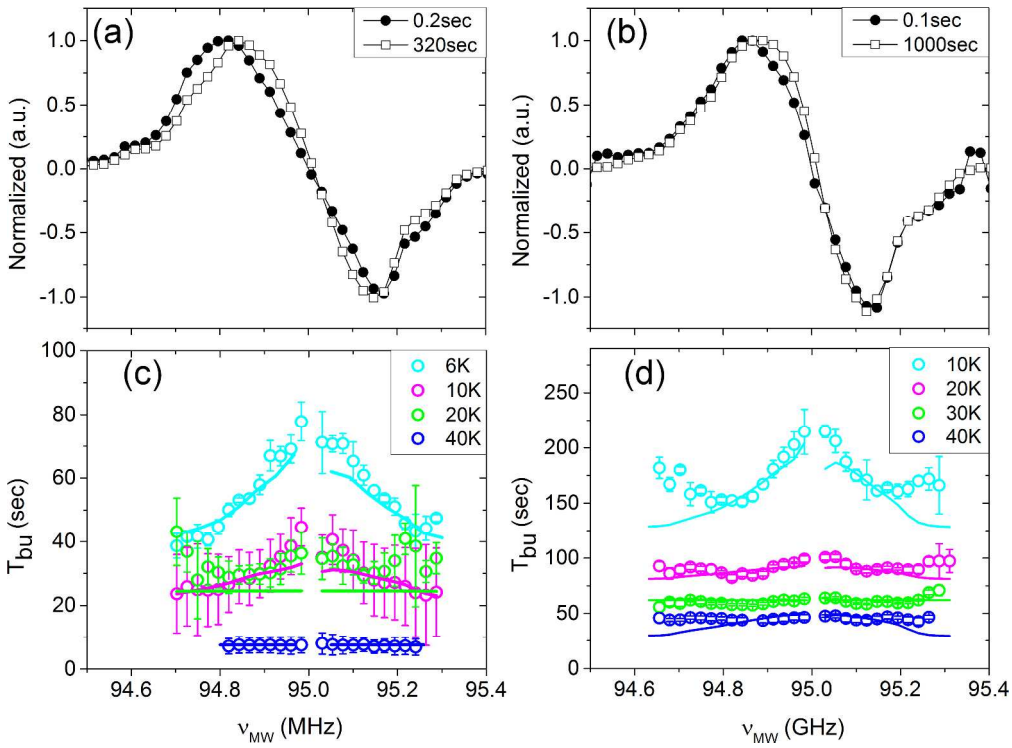

923x679mm (120 x 120 DPI)

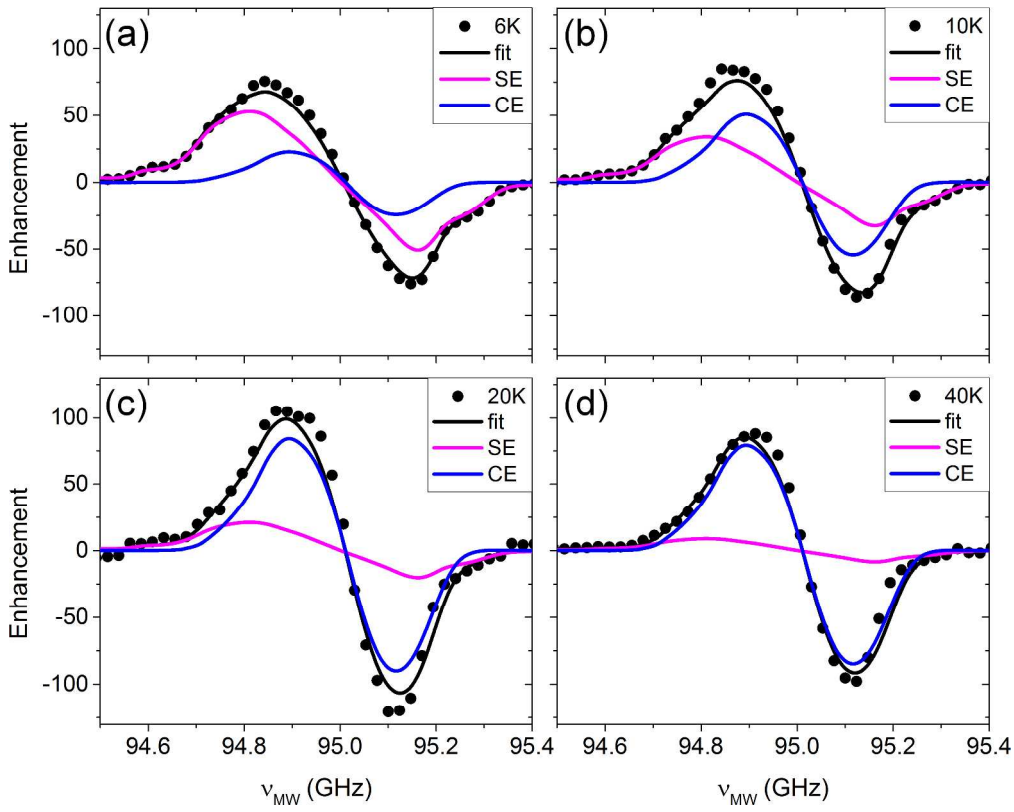

852x679mm (120 x 120 DPI)

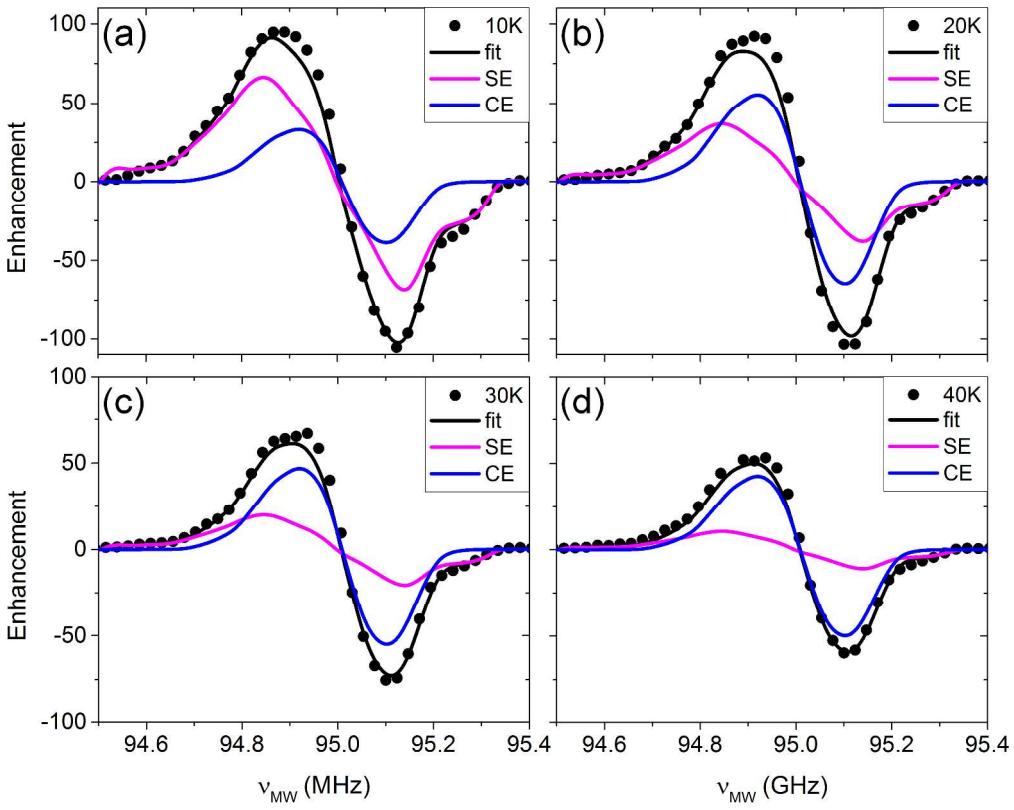

854x679mm (120 x 120 DPI)

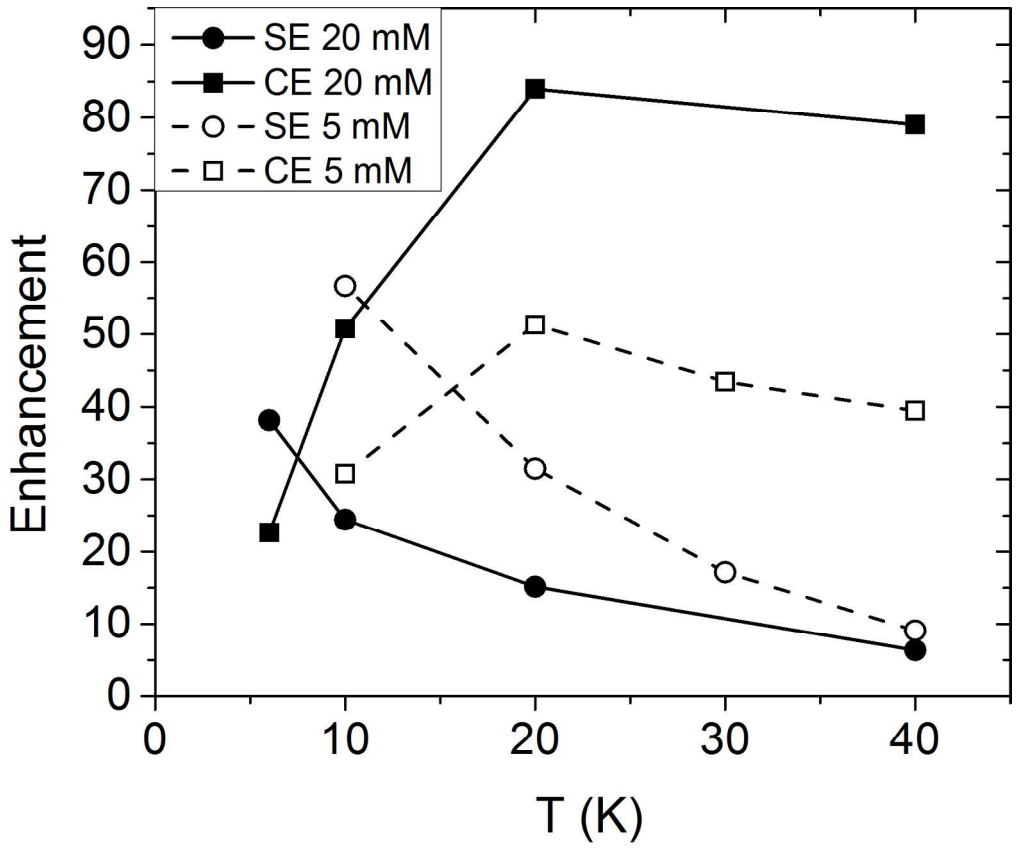

430x358mm (120 x 120 DPI)

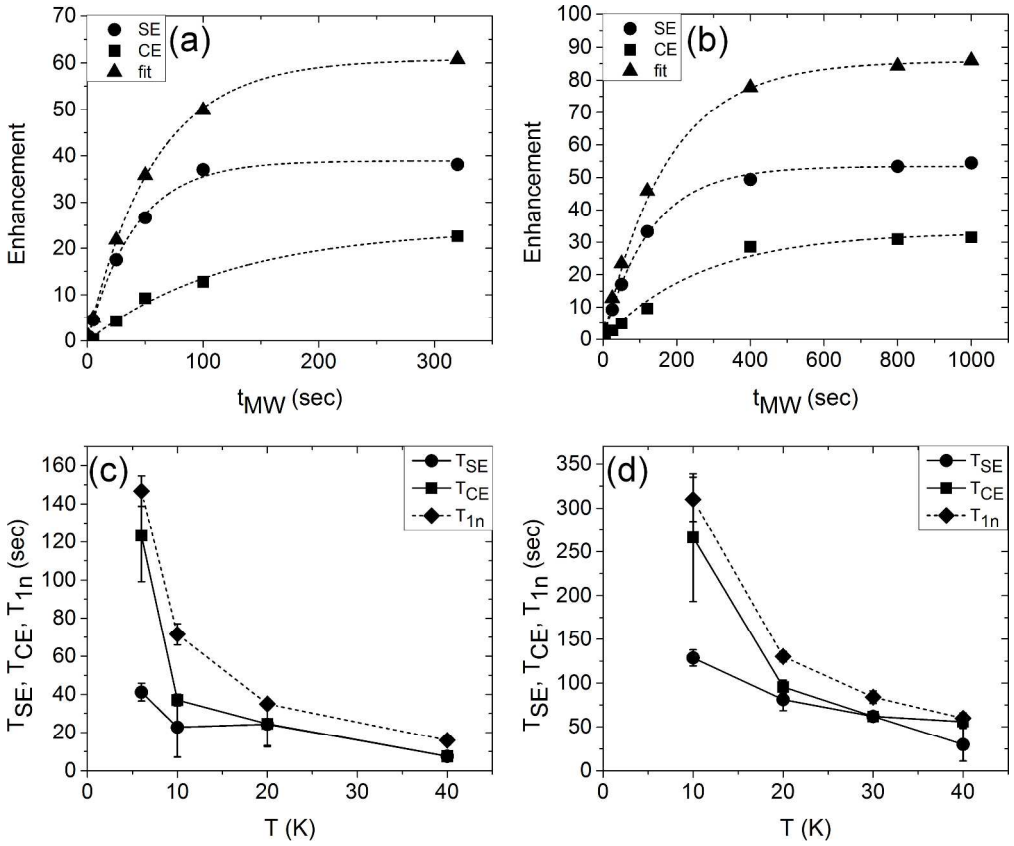

909x759mm (120 x 120 DPI)

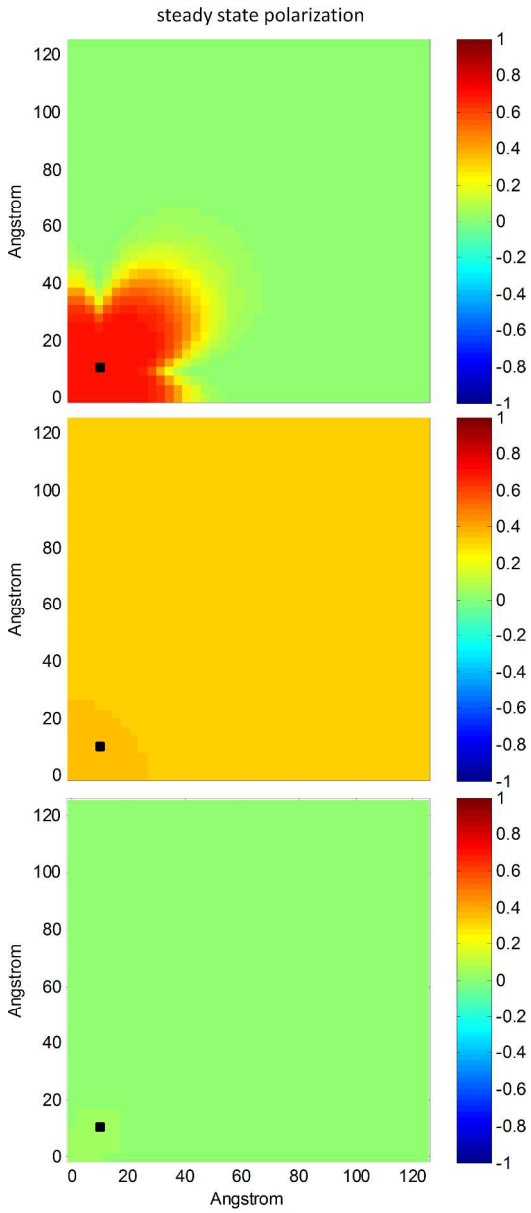

523x1213mm (120 x 120 DPI)

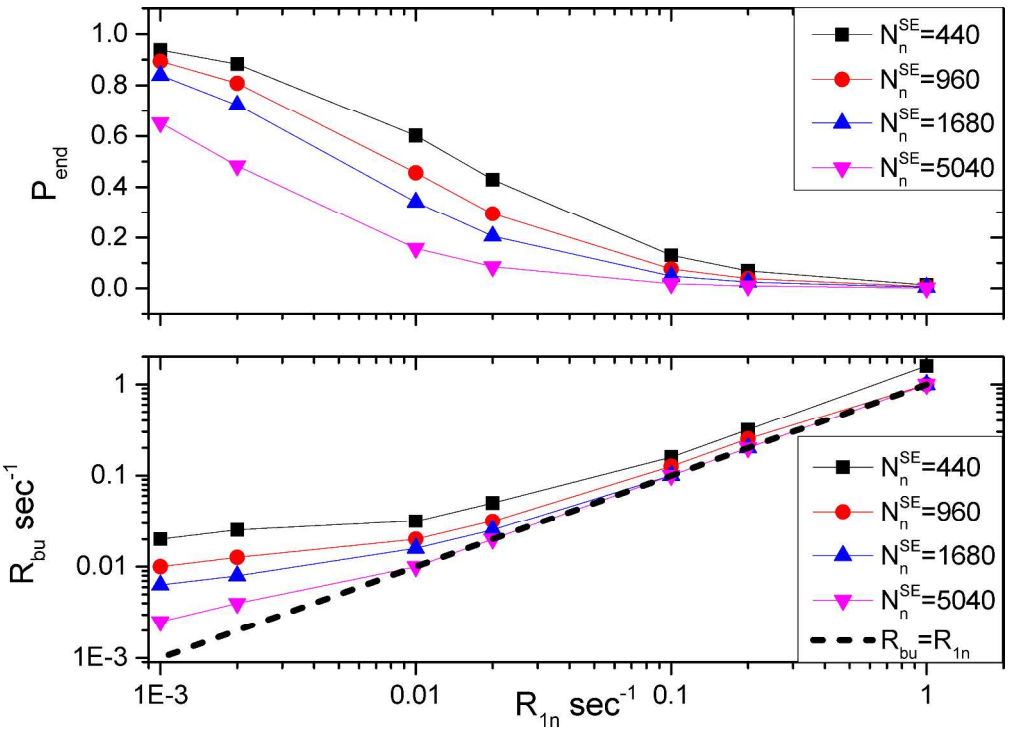

776x557mm (120 x 120 DPI)